

## Effect of undercooling on clinopyroxene crystallization in a high K basalt: Implications for magma dynamics at Stromboli volcano

F. Colle <sup>a,\*</sup>, M. Masotta <sup>b,c</sup>, S. Costa <sup>b</sup>, S. Mollo <sup>d,e</sup>, P. Landi <sup>f</sup>, A. Pontesilli <sup>e</sup>, S. Peres <sup>g</sup>, L. Mancini <sup>h</sup>

<sup>a</sup> Dipartimento di Scienze Chimiche, della Vita e della Sostenibilità Ambientale, Università di Parma, Campus Universitario—Parco Area delle Scienze 157A, 43124 Parma, Italy

<sup>b</sup> Dipartimento di Scienze della Terra, Università di Pisa, via S. Maria 53, 56126 Pisa, Italy

<sup>c</sup> CISUP - Centro per l'Integrazione della Strumentazione Università di Pisa, via Lungarno Pacinotti 43, Pisa, Italy

<sup>d</sup> Dipartimento di Scienze della Terra, Sapienza - Università di Roma, P.le Aldo Moro 5, 00185 Roma, Italy

<sup>e</sup> Istituto Nazionale di Geofisica e Vulcanologia, Sezione di Roma, Via di Vigna Murata 605, 00143 Rome, Italy

<sup>f</sup> Istituto Nazionale di Geofisica e Vulcanologia, Sezione di Pisa, Via Cesare Battisti, 53, 56125 Pisa, Italy

<sup>g</sup> Department für Lithosphärenforschung, Universität Wien, Althanstraße 14, A-1090 Wien, Austria

<sup>h</sup> ZAG - Slovenian National Building and Civil Engineering Institute, Dimičeva ulica 12, 1000 Ljubljana, Slovenia

### ARTICLE INFO

#### Keywords:

Clinopyroxene  
Undercooling  
Hourglass  
Crystallization  
Microtomography  
Stromboli

### ABSTRACT

We present undercooling ( $\Delta T$ ) experiments aimed at investigating the effect of growth kinetics on the textural and compositional evolution of clinopyroxene crystals growing from a high-K basalt erupted during the 2003 paroxysm of Stromboli volcano (Italy). The experiments were performed at  $P = 350$  MPa,  $T = 1050$ – $1210$  °C,  $H_2O_{melt} = 0$ – $3$  wt%, and  $fO_2 = Ni-NiO + 1.5$  buffer. An initial stage of supersaturation was imposed to the melt under nominally anhydrous ( $\Delta T_{anh} = 10$ – $150$  °C) and hydrous ( $\Delta T_{hyd} = 25$ – $125$  °C) conditions. Afterwards, this supersaturation state was mitigated by melt relaxation phenomena over an annealing time of 24 h. Results show that plagioclase is the liquidus mineral phase of the high-K basalt at  $\Delta T_{anh} = 10$  °C and dominates the phase assemblage as the degree of undercooling increases. Conversely, clinopyroxene and spinel co-saturate the melt at  $\Delta T_{hyd} = 25$  °C, followed by the subordinate formation of plagioclase. At  $\Delta T_{anh/hyd} \leq 50$  °C, the textural maturation of clinopyroxene produces polyhedral crystals with  $\{-111\}$  (hourglass) and  $\{hk0\}$  (prism) sectors typical of a layer-by-layer growth mechanism governed by an interface-controlled crystallization regime. At  $\Delta T_{anh/hyd} \geq 75$  °C, the attainment of dendritic and skeletal morphologies testifies to the establishment of diffusion-limited reactions at the crystal-melt interface. 3D reconstructions of synchrotron radiation X-ray microtomographic data reveal a composite growth history for clinopyroxene crystals obtained at  $\Delta T_{anh/hyd} \geq 95$  °C. The early stage of melt supersaturation produces rosette-like structures composed of dendritic branches of clinopyroxene radiating from a common spinel grain, which acts as surface for heterogeneous nucleation. As diffusive relaxation phenomena progress over the annealing time, the elongate dendrites that constitute the inner crystal domain are partially infilled by the melt and develop skeletal overgrowths in the outer domain. With the increasing degree of undercooling,  ${}^TAl$  and  ${}^{M1}Ti$  cations are progressively incorporated in the lattice site of clinopyroxene at the expense of  ${}^TSi$  and  ${}^{M1}Mg$  cations. Because of the effect of  $H_2O_{melt}$  on the liquidus depression and melt depolymerization, crystals obtained at  $\Delta T_{hyd}$  are also more enriched in  ${}^TAl$  and  ${}^{M1}Ti$  and depleted in  ${}^TSi$  and  ${}^{M1}Mg$  than those growing at  $\Delta T_{anh}$ . The emerging picture is that the morphological and geochemical evolution of clinopyroxene is mutually controlled by the combined effects of melt supersaturation and relaxation phenomena. A new empirical relationship based on the cation exchange reactions in the lattice site of clinopyroxene is finally proposed to estimate the degree of undercooling governing the crystallization of augitic phenocrysts erupted during normal and violent explosions at Stromboli.

\* Corresponding author.

E-mail address: [fabio.colle@unipr.it](mailto:fabio.colle@unipr.it) (F. Colle).

<https://doi.org/10.1016/j.lithos.2023.107327>

Received 5 April 2023; Received in revised form 20 July 2023; Accepted 11 August 2023

Available online 16 August 2023

0024-4937/© 2023 The Authors. Published by Elsevier B.V. This is an open access article under the CC BY-NC-ND license (<http://creativecommons.org/licenses/by-nc-nd/4.0/>).

## 1. Introduction

Crystallization is a fundamental process determining the chemical evolution of magmas and influencing their rheology in subvolcanic environments (Arzilli et al., 2022; Hammer, 2008; Kurokawa et al., 2022). The dynamic interplay between interface-controlled and diffusion-controlled growth regimes is settled by cooling and degassing phenomena taking place during the ascent of magmas towards the surface (Hammer, 2008; Mollo and Hammer, 2017). These phenomena impose a certain degree of undercooling ( $\Delta T$ ) to the crystal-melt interface, which is expressed as the difference between the liquidus temperature of the melt and the final resting temperature at which crystallization takes place (Kirkpatrick, 1981).  $\Delta T$  is the driving force for crystallization and its magnitude is proportional to the degree of supersaturation of a mineral phase in the melt. A supersaturated melt evolves towards bulk thermodynamic equilibrium as diffusive relaxation phenomena reduce the concentration gradients that develop at the crystal-melt interface. Once the rate at which atoms are attached from the melt onto the crystalline layer is balanced by an equivalent detachment rate, the net change in the number of atoms in the crystal is zero and the condition of crystal growth ceases (Lasaga, 1998; Sunagawa, 2005).

Several experimental studies published in the last decades have examined the phenomenological aspects related to the kinetics of clinopyroxene textural and compositional changes under dynamic crystallization conditions (Arzilli et al., 2015, 2019, 2022; Coish and Taylor, 1979; Di Fiore et al., 2022; Gamble and Taylor, 1980; Hammer, 2006; Kouchi et al., 1983; Lofgren et al., 2006; MacDonald et al., 2022; Masotta et al., 2020; McKay et al., 1994; Mollo et al., 2010, 2013a, 2013b; Moschini et al., 2021; Pontesilli et al., 2019; Tsuchiyama, 1985). Clinopyroxene is one of the most common minerals of mafic volcanic rocks and its textural and compositional evolution has been recognized as the direct expression of the role played by crystal growth kinetics during the dynamic ascent of magmas across polybaric-polythermal crustal regions and within the conduits of active volcanoes in Italy (Armienti et al., 2013; Costa et al., 2023; Di Stefano et al., 2020; Downes, 1974; Duncan and Preston, 1980; Mollo et al., 2018, 2020, 2022; Palummo et al., 2021; Petrone et al., 2018, 2022; Ubide et al., 2019; Ubide and Kamber, 2018).

Stromboli represents a noteworthy example of open conduit volcano where the growth history of clinopyroxene phenocrysts is associated to abrupt changes in  $\Delta T$  caused by cooling, decompression, and degassing phenomena, resulting from the continuous recharge, crystallization, and eruption of basaltic magmas (Di Stefano et al., 2020; Petrone et al., 2018, 2022). The architecture of this chemically and physically perturbed plumbing system is envisaged as a vertically-extended magma column persistently infilled by primitive and volatile-rich low-porphyrific (*Lp*) magmas rising from depth and mixing with more evolved and degassed high-porphyrific (*Hp*) magmas stored at shallow crustal levels (Bertagnini et al., 2003, 2008; Francalanci et al., 2004, 2012; Landi et al., 2006, 2008, 2009; Métrich et al., 2010). As a result, clinopyroxene phenocrysts develop complex zoning patterns with diopsidic antecryst cores and diopsidic bands in equilibrium with *Lp*-magmas, which are overgrown by augitic mantles and rims herald of crystallization from *Hp*-magmas (Di Stefano et al., 2020). Textural and compositional attributes of clinopyroxene phenocrysts indicate multi-stage crystallization phenomena across the Stromboli *Lp*-*Hp*-reservoirs, where efficient remobilization of the mush between 2003 and 2007 led to a rejuvenated plumbing system configuration in 2019 (Di Stefano et al., 2020; Petrone et al., 2018, 2022).

In this study we present undercooling crystallization experiments carried out on a high-K basaltic melt representative of the primitive *Lp*-magma erupted at Stromboli during the 2003 violent explosion. The experimental conditions were chosen to decipher the control of  $\Delta T$  (varying from 10 to 150 °C) on clinopyroxene growth kinetics during the solidification of anhydrous and hydrous magmas. Textural analysis based on 3D reconstructions of synchrotron radiation X-ray

microtomographic data provide insight into the phenomenological aspects related to the kinetics of clinopyroxene growth. Furthermore, the compositional changes of experimental clinopyroxene crystals and melts are used to provide an interpretation of the dynamics of magmas feeding the explosive activity at Stromboli volcano.

## 2. Materials and methods

### 2.1. Experimental methods

The experimental work was conducted at the High Pressure-High Temperature Laboratory of the Department of Earth Sciences at University of Pisa (Italy). A scoria, representative of the *Lp*-magma erupted during the 5 April 2003 violent explosion at Stromboli volcano, was selected as starting material for the experiments. The erupted product consists of a high-K basalt with a low porphyritic index (<5 vol%) and a glassy groundmass (Métrich et al., 2005). The scoria was first crushed into fine powder using an agate mortar and loaded into a Fe-pre-saturated Pt-crucible. The crucible containing the powder was introduced into a chamber furnace pre-heated at 1400 °C and held at this temperature for 1 h before being quenched by direct drop in deionized water. The resulting glass was removed from the crucible and crushed into a fine powder using an agate mortar. A small portion of the glass was inspected with the scanning electron microscope to verify the absence of crystalline phases. The average chemical composition of the starting glass is reported in the supplementary material (Table S1 in the Supplementary Material 2).

Undercooling experiments were carried out in a non-end loaded piston cylinder (“QUICKpress” design by Depths of the Earth Co.) using a low pressure 25 mm NaCl-pyrex-graphite-MgO assembly (Masotta et al., 2012). For nominally anhydrous undercooling experiments (hereafter  $\Delta T_{anh}$ ), the Pt-capsule (3.0 mm outer diameter, 2.7 mm inner diameter) was filled with the powdered starting glass. For hydrous undercooling experiments (hereafter  $\Delta T_{hyd}$ ), 2 or 3 wt% of deionized H<sub>2</sub>O were added with a micro-syringe to the powdered starting glass loaded into the Pt-capsule. An instantaneous freezing spray was employed to rapidly cool the capsule and prevent H<sub>2</sub>O evaporation. To assess any potential weight loss, the capsule was weighed before and at the end of the experiment, by placing it in oven at 110 °C for several hours. No weight loss has been observed. Pyrophyllite powder was used as support pressure media for  $\Delta T_{hyd}$  experiments to minimize H<sub>2</sub>O loss from the Pt-capsule walls, whereas a borosilicate glass powder was used for  $\Delta T_{anh}$  experiments. Glass analysis was cautiously carried out at the central portion of the experimental samples, although no loss of Fe by solution in the Pt-capsule has been measured in the glass close to the capsule.

The intrinsic oxygen fugacity imposed by assembly to the bulk chemical system is about 1.5 log units above the Ni-NiO buffer (i.e., NNO + 1.5), as quantified by Masotta et al. (2012). Re-equilibration of the iron speciation in the starting glass has been observed to take place within a few hours, when the redox state of the system shifts from air to NNO + 1.5 (cf. Mollo et al., 2013). For each experiment, the assembly was cold-pressurized to 350 MPa for 30 min before heating to a super-liquidus temperature of 1300 °C at a rate of 80 °C/min. After 30 min at 1300 °C, a final target temperature variable from 1050 to 1210 °C (Table 1) was reached by cooling the experiment at 80 °C/min. This early effect of melt supersaturation was mitigated by diffusive relaxation due to an annealing time of 24 h (cf. Masotta et al., 2020). The temperature was monitored by a factory-calibrated C-type thermocouple with uncertainty of  $\pm 3$  °C. At the end of each experiment, the bulk chemical system was frozen-in through an isobaric quench performed at a cooling rate of  $\sim 100$  °C/s.

As stated above (see §1), the degree of undercooling has been calculated as the difference between the liquidus temperature of the melt and the final resting temperature of the system, yielding  $\Delta T_{anh} = 10\text{--}150$  °C and  $\Delta T_{hyd} = 25\text{--}125$  °C (Table 1). The liquidus temperatures of the silicate melt at anhydrous and hydrous conditions, and at oxygen fugacity

**Table 1**

List of the experiments reporting the experimental conditions and the mineral phase assemblage determined by image analysis (see text for additional information).

Experiment	$T_{\max}$ (°C)	CR (°C/min)	$T_{\text{rest}}$ (°C)	Time $T_{\text{rest}}$ (h)	P (MPa)	H <sub>2</sub> O <sub>added</sub> (wt%)	$\Delta T$ (°C)	Mineral assemblage (vol%)
Anhydrous experiments								
SB03-1210a	1300	80	1210	24	350	0.0	–	Gl(100)
SB03-1190a	1300	80	1190	24	350	0.0	10	Gl(90), Pl(10)
SB03-1175a	1300	80	1175	24	350	0.0	25	Gl(76), Timt(Tr), Cpx(6), Pl(18)
SB03-1150a	1300	80	1150	24	350	0.0	50	Gl(55), Timt(3), Cpx(16), Pl(26)
SB03-1125a	1300	80	1125	24	350	0.0	75	Gl(45), Timt(3), Cpx(22), Pl(30)
SB03-1100a	1300	80	1100	24	350	0.0	100	Gl(37), Timt(3), Cpx(26), Pl(34)
SB03-1050a	1300	80	1050	24	350	0.0	150	Gl(26), Timt(2), Cpx(31), Pl(41)
Hydrous experiments								
SB03-1180b	1300	80	1180	24	350	2.0	–	Gl(100)
SB03-1150b	1300	80	1150	24	350	2.0	25	Gl(84), Timt(1), Cpx(15)
SB03-1125b	1300	80	1125	24	350	2.0	50	Gl(67), Timt(2), Cpx(23), Pl(8)
SB03-1100b	1300	80	1100	24	350	2.0	75	Gl(59), Timt(3), Cpx(25), Pl(13)
SB03-1050b	1300	80	1050	24	350	2.0	125	Gl(57), Timt(3), Cpx(24), Pl(16)
SB03-1050c	1300	80	1050	24	350	3.0	95	Gl(49), Timt(3), Cpx(28), Pl(20)

corresponding to that of the NNO + 1.5 buffer, were determined using PhasePlot 2.0 (<https://phaseplot.org>), a software package based on rhyolite-MELTS database (Ghiorso and Sack, 1995; Gualda et al., 2012). For the anhydrous melt, a liquidus temperature of 1230 °C is predicted, whereas for the hydrous melts with 2 and 3 wt% H<sub>2</sub>O, the liquidus temperatures are 1175 °C and 1155 °C, respectively. Notably, the liquidus temperature of the hydrous melt with 2 wt% H<sub>2</sub>O is bracketed by the experiment performed at superliquidus temperature (ST03-1180b; see also Fig. F1 in the Supplementary Material 1) and the experiment performed at 1150 °C (ST03-1150b), showing clinopyroxene as liquidus phase. Nonetheless, the liquidus temperature predicted at anhydrous conditions is not consistent with the anhydrous experiment performed at 1210 °C (ST03-1210a), which is characterized by only glass. For the anhydrous melt we thus consider a liquidus temperature of 1200 °C, determined as the thermal state between the superliquidus experiment (ST03-1210a) and the experiment performed at 1190 °C (ST03-1190a).

## 2.2. Analytical methods

Backscattered electron (BSE) images of the experimental products were collected at the Centre for Instrument Sharing at the University of Pisa (CISUP), with a FEI Quanta 450 field emission gun scanning electron microscope (FE-SEM), equipped with an XRF energy-dispersive (EDS) detector. The operating conditions used are 15 kV acceleration voltage and 10 nA beam current. The ImageJ software (<https://imagej.net>) package was used for image processing (i.e., thresholding and segmentation) and phase abundance quantification. Because of the small number and relatively large size (up to mm) of crystals formed in experimental charges, the maximum crystal length ( $L_{\max}$ ) of each phase was inferred from the length of the major axis of the ellipse fitting the largest exposed crystal.

Microchemical analyses were performed at the High Pressure-High Temperature Laboratory of Istituto Nazionale di Geofisica e Vulcanologia (INGV-Rome, Italy) using a JEOL-JXA8200 electron probe microanalyzer (EPMA) with combined EDS-WDS (five spectrometers with twelve crystals). Data were collected using 15 kV accelerating voltage and 10 nA beam current. For glasses, a slightly defocused electron beam with a diameter of 5  $\mu\text{m}$  was used, with a counting time of 15 s on peak and 5 s on low and high background. For crystals, the beam size was 2  $\mu\text{m}$  with a counting time of 20 s on peak and 10 s on low and high background. Calibration used a range of standards from Micro-Analysis Consultants (MAC; <http://www.macstandards.co.uk>): albite (Si, Al, and Na), forsterite (Mg), augite (Fe), apatite (Ca and P), orthoclase (K), rhodonite (Mn), and rutile (Ti). Sodium and potassium were analysed first to minimize alkali migration effects. Smithsonian augite (Jarosewich et al., 1980) and MAC augite were used as quality monitor standards and for the calculation of accuracy and precision. Accuracy

was better than 5% except for elements with abundances below 1 wt%, for which accuracy was better than 10%. Chemical analyses of glasses and mineral phases are reported in the supplementary material (Tables S1, S2 and S3 in the Supplementary Material 2).

Three fragments ( $\sim 2 \text{ mm}^3$ ) of experimental samples performed at the same target temperature of 1050 °C but different degree of undercooling (i.e., SB03-1050a with  $\Delta T_{\text{anh}} = 150$  °C; SB03-1050b with  $\Delta T_{\text{hyd}} = 125$  °C; SB03-1050c with  $\Delta T_{\text{hyd}} = 95$  °C) were removed from the Pt-capsule and analysed with a synchrotron radiation X-ray computed microtomography (SR- $\mu\text{CT}$ ) at the SYRMEP beamline of Elettra (Elettra Sincrotrone Trieste). A filtered polychromatic X-ray beam (filters = 1.5 mm Si + 1 mm Al) was used. The detector consisted of a 16-bit, water-cooled, sCMOS macroscope camera (Hamamatsu C11440-22C) with a 2048  $\times$  2048 pixels chip coupled through a high numerical aperture optics to a 17  $\mu\text{m}$ -thick GGG:Eu scintillator screen. Scans were acquired in propagation-based phase-contrast mode by setting a sample-to-detector distance of 150 mm. For each sample, 900 projections were acquired over a total scan angle of 180° and with an exposure time/projection of 2.5 s. The tomographic reconstruction was performed by using the SYRMEP Tomo Project (STP) software suite developed at Elettra (Brun et al., 2015). Axial slices were reconstructed by using the filtered back-projection algorithm and an isotropic voxel size of 2.5  $\mu\text{m}$ . Volume visualization with volume rendering procedures was performed with the Dragonfly software (<https://www.theobjects.com/index.html>).

## 3. Results

### 3.1. Textural features of experimental products

Under anhydrous crystallization conditions, the inferred liquidus temperature of 1200 °C is bracketed by the crystal-free and crystal-bearing experiments carried out at 1210 °C and 1190 °C, respectively (Table 1). The crystal content overall increases from 10 vol% in the experiment at  $\Delta T_{\text{anh}} = 10$  °C to 74 vol% in the experiment performed at  $\Delta T_{\text{anh}} = 150$  °C. At the smallest value of  $\Delta T_{\text{anh}} = 10$  °C, plagioclase is the liquidus mineral phase and grows as large ( $L_{\max} = 1 \text{ mm}$ ) tabular crystals partially infilled with melt. At  $\Delta T_{\text{anh}} = 25$  and 50 °C, plagioclase ( $L_{\max} = 800 \mu\text{m}$ ) is followed by clinopyroxene ( $L_{\max} = 600 \mu\text{m}$ ) and spinel ( $L_{\max} = 30 \mu\text{m}$ ), all mineral phases showing euhedral morphologies (Fig. 1a, b). Clinopyroxene is sector-zoned, with hourglass and prism faces characterized by dark and bright BSE intensities, respectively (Fig. 1a, b). At  $\Delta T_{\text{anh}} \geq 75$  °C, plagioclase ( $L_{\max} = 400\text{--}600 \mu\text{m}$  depending on  $\Delta T_{\text{anh}}$ ) and clinopyroxene ( $L_{\max} = 300\text{--}500 \mu\text{m}$  depending on  $\Delta T_{\text{anh}}$ ) are dominantly skeletal and dendritic, respectively, showing more elongate forms (Fig. 1c). It is worth noting that dendritic clinopyroxene crystals obtained at  $\Delta T_{\text{anh}} = 150$  °C are arranged to form radial structures around spinel crystals (Fig. 1c).

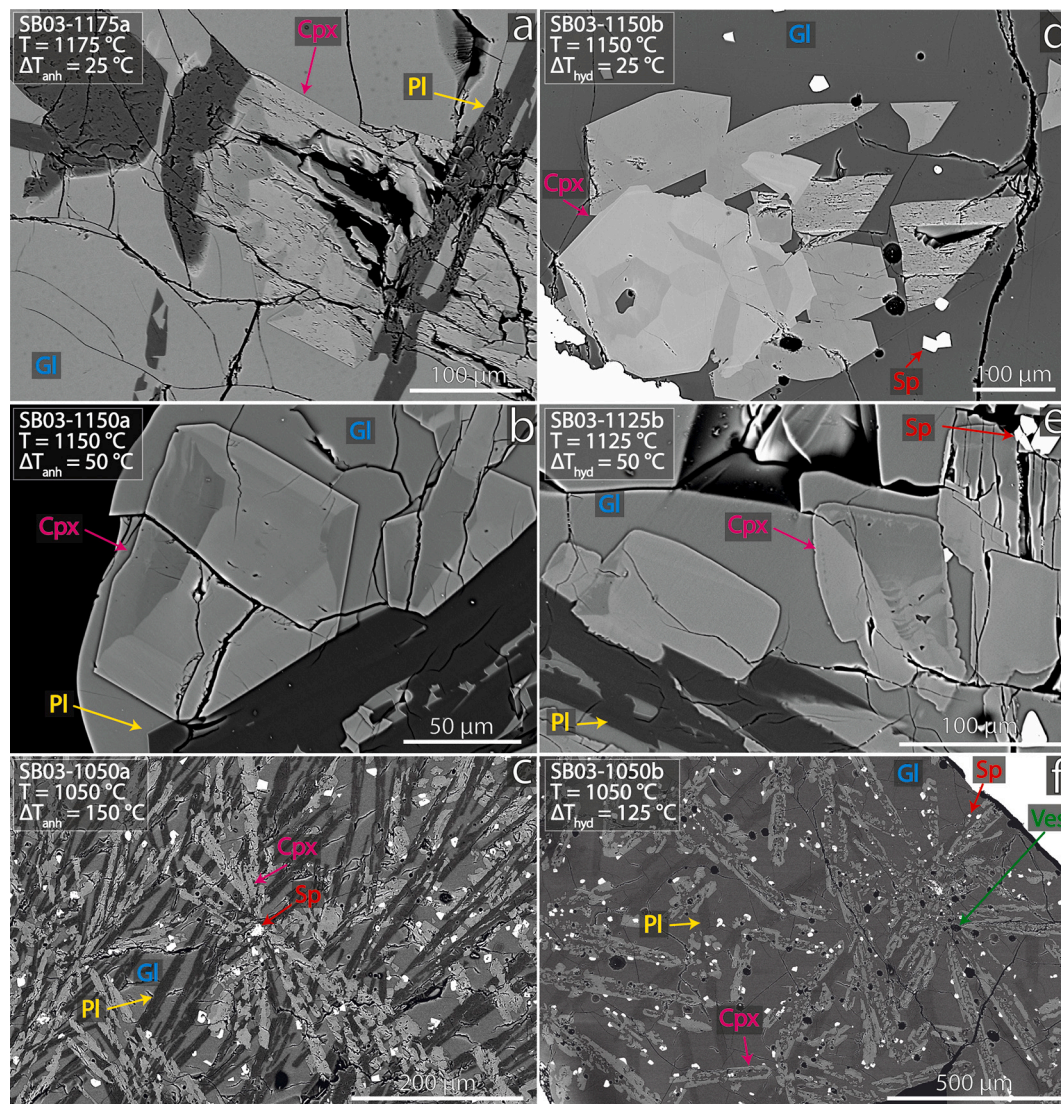


**Fig. 1.** Backscattered electron (BSE) images of undercooling experiments performed at anhydrous (a-c) and hydrous (d-f) conditions. Clinopyroxene crystals formed at  $\Delta T_{anh,hyd} \leq 50$  °C are euhedral and show a hourglass sector zoning (a,b,d,e). At  $\Delta T_{anh} = 150$  °C and  $\Delta T_{hyd} = 95$  °C clinopyroxene crystals are characterized by dendritic forms often arranged radially around spinel crystals (c,f).

Under hydrous crystallization conditions, the liquidus temperature of 1175 °C estimated using PhasePlot is bracketed by the experiments carried out at 1180 °C (crystal-free charge) and 1150 °C (crystal-bearing charge) (Table 1). The crystal content overall increases from 16 vol% in the experiment performed at  $\Delta T_{hyd} = 25$  °C to 51 vol% in the experiment performed at  $\Delta T_{hyd} = 95$  °C. Differently from  $\Delta T_{anh}$  experiments, the effect of dissolved H<sub>2</sub>O at  $\Delta T_{hyd} = 25$  °C destabilizes the crystallization of plagioclase as liquidus mineral phase in favor of clinopyroxene ( $L_{max} = 800$  μm) and spinel ( $L_{max} = 50$  μm) co-saturation (Table 1). Plagioclase ( $L_{max} = 1$  mm) joins to the phase assemblage at  $\Delta T_{hyd} = 50$  °C (Fig. 1e). In general, the morphology of crystals formed at  $\Delta T_{hyd} \leq 50$  °C resembles that observed for crystals segregated at  $\Delta T_{anh} \leq 50$  °C, including the sector zoning of clinopyroxene (Fig. 1d,e). At  $\Delta T_{hyd} \geq 75$  °C, clinopyroxene ( $L_{max} = 600$  μm depending on  $\Delta T_{hyd}$ ) and plagioclase ( $L_{max} = 400$ –500 μm depending on  $\Delta T_{hyd}$ ) are dominantly dendritic and skeletal, respectively. Notably, as already described for the experiment performed at  $\Delta T_{anh} = 150$  °C, dendritic clinopyroxene crystals appear arranged to form radial structures around spinel crystals in the experiments performed at  $\Delta T_{hyd} \geq 95$  °C (Fig. 1f).

### 3.2. 3D reconstruction of clinopyroxene textures

The 3D reconstructions of SR-μCT clinopyroxene data obtained at  $\Delta T_{hyd} = 95$  and 125 °C are illustrated in Fig. 2. Individual clinopyroxene crystals show two distinct textural domains: 1) an inner domain characterized by dendritic branches and 2) an outer domain characterized by euhedral/skeletal morphologies (Fig. 2a,b). This textural evolution suggests that clinopyroxene growth first occurs under a high supersaturation condition, which diminishes as growth proceeds over the annealing time (Sunagawa, 2005). Because of progressive decrease in melt supersaturation, early-formed dendritic branches with uneven faces (i.e., fast growth rate) start to assume a polyhedral form bounded by flat faces (i.e., decreasing growth rate) upon the effect of melt relaxation and infilling. According to Sunagawa (2005), outer skeleton forms and inner dendritic branches can be observed when a polyhedral clinopyroxene crystal is bisected. Furthermore, in hydrous experiments, vesicles with size (diameter) ranging from 10 to 50 μm develop in proximity of the dendritic branches, suggesting the establishment of H<sub>2</sub>O concentration gradients at the melt interface, next to the rapidly grown dendrites (Fig. 2a,b).

Irrespective of anhydrous and hydrous crystallization conditions,

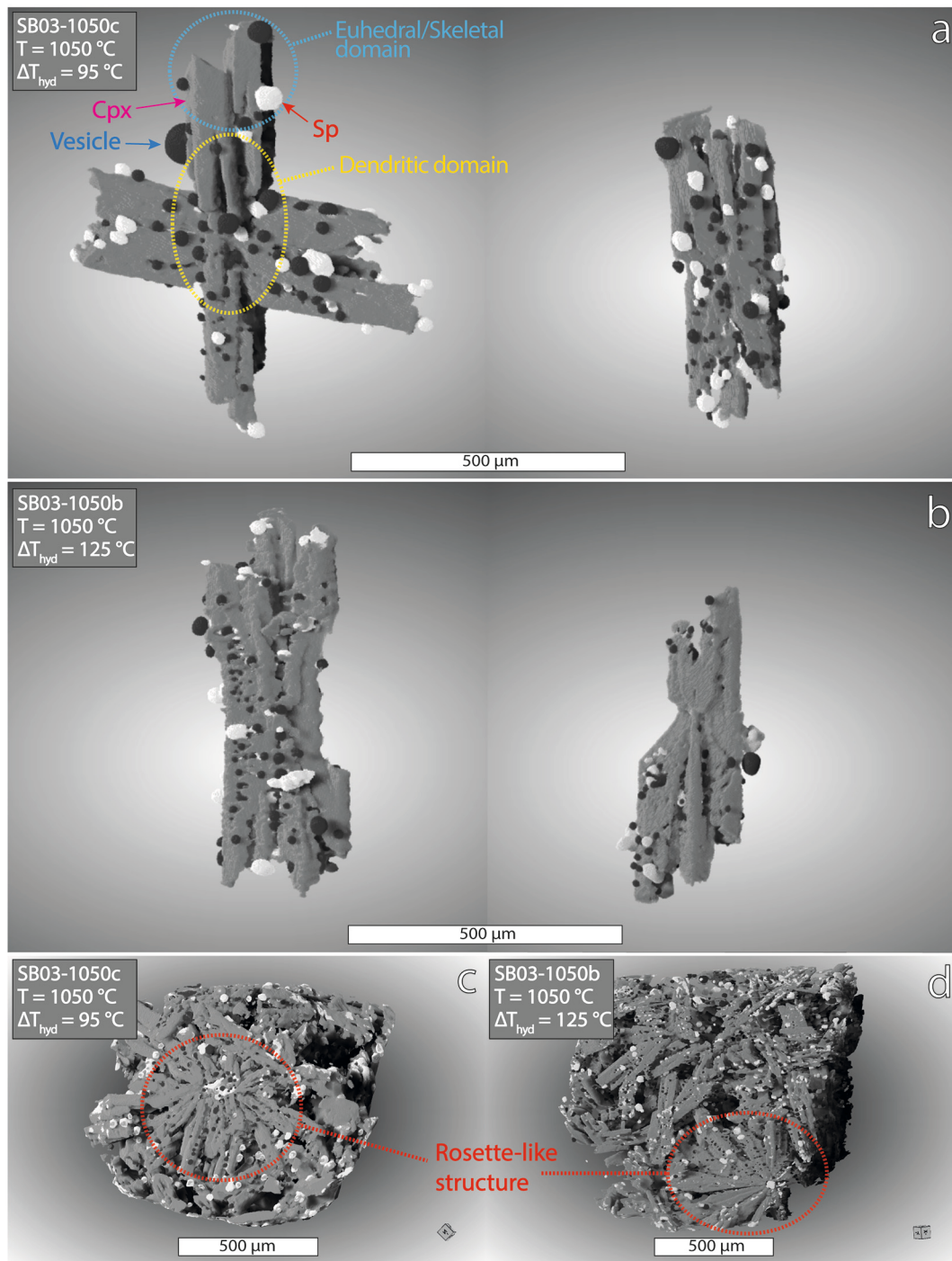


**Fig. 2.** Volume rendering of individual crystals (a,b) and cluster (c) of clinopyroxene obtained using SR- $\mu$ CT data reconstructed with an isotropic voxel size of 2.5  $\mu$ m and isosurface rendering after segmentation of vesicles (coloured in dark grey) and spinel (coloured in white); yellow and blue circles indicate the inner dendritic domain and the outer euhedral/skeletal domain, respectively, whereas red circle indicate a rosette-like structure. (For interpretation of the references to colour in this figure legend, the reader is referred to the web version of this article.)

several clinopyroxene crystals do not grow as individual forms but rather produce rosette-like structures composed of dendritic branches and skeletal overgrowths radiating from a common spinel crystal acting as nucleation center (Fig. 2c,d). Therefore, we speculate that clinopyroxene crystals may either homogeneously nucleate from the melt via a spontaneous crystallization reaction or may heterogeneously nucleate onto the spinel grain due to the presence of a catalyst surface which lowers the energetic barrier for the formation of a critical nucleus.

### 3.3. Mineral and glass chemistry

Fig. 3 shows the variation of  $^T\text{Si}$ ,  $^T\text{Al}$ ,  $^{\text{M1}}\text{Mg}$ , and  $^{\text{M1}}\text{Ti}$  cations in the lattice site of clinopyroxene as a function of  $\Delta T_{\text{anh}}$  and  $\Delta T_{\text{hyd}}$ . As a general rule, the decrease of  $^T\text{Si}$  and  $^{\text{M1}}\text{Mg}$  with increasing  $\Delta T_{\text{anh/hyd}}$  is counterbalanced by the increase of  $^T\text{Al}$  and  $^{\text{M1}}\text{Ti}$  (Table S2 in the Supplementary Material 2). Despite this intracrystalline variation, the composition of experimental clinopyroxene is very similar to that of mantle and rim domains of natural clinopyroxene phenocrysts contained

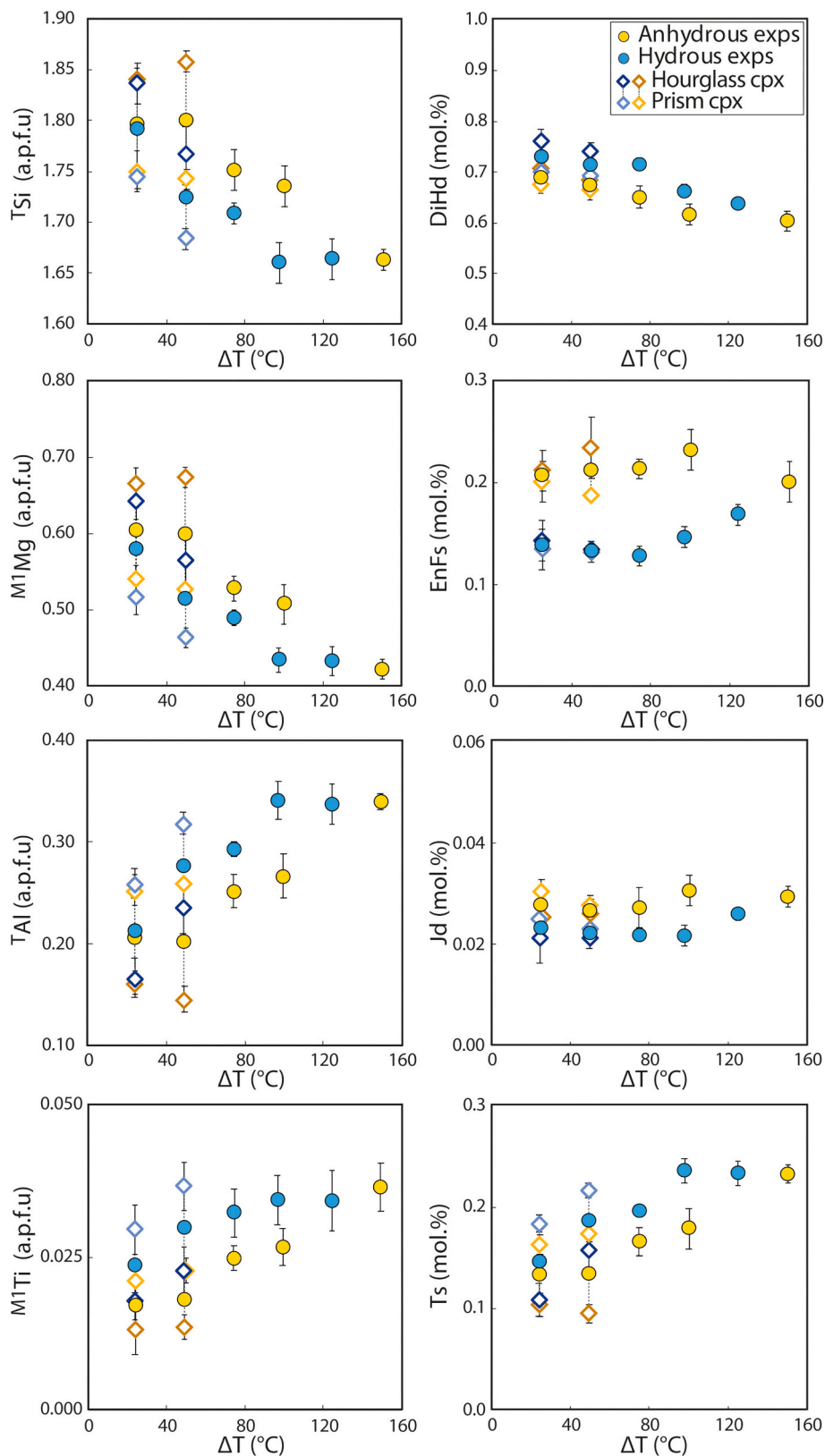


**Fig. 3.** Compositional variation of experimental clinopyroxene with varying degrees of  $\Delta T_{anh}$  (yellow circles) and  $\Delta T_{hyd}$  (blue circles). The variation of  ${}^T\text{Si}$ ,  ${}^T\text{Al}$ ,  ${}^{M1}\text{Mg}$ , and  ${}^{M1}\text{Ti}$  cations (atoms per formula unit) in the lattice site of clinopyroxene is reported in the left column, whereas the variation of the components DiHd, EnFs, Jd and Ts (i.e., the sum of Ca-Tschermak and CaTi-Tschermak components) is reported in the right column. For sector zoned clinopyroxene, filled circles represent the average composition between hourglass (HG) and prism (PR) sectors, indicated by open diamonds. (For interpretation of the references to colour in this figure legend, the reader is referred to the web version of this article.)

in both *Lp*- and *Hp*-magmas at Stromboli (Fig. F2 in the Supplementary Material 1), classified in literature as augitic mantles and rims (Petroni et al., 2022 and references therein). The depolymerizing effect of  $\text{H}_2\text{O}$  on the melt phase enhances the formation of  ${}^T\text{Al}$ - ${}^{M1}\text{Ti}$ -rich crystals formed at  $\Delta T_{hyd}$  with respect to  ${}^T\text{Si}$ - ${}^{M1}\text{Mg}$ -rich crystals obtained at  $\Delta T_{anh}$ . A low

activity of silica in the melt favours the substitution of aluminum for silicon in T-site, with consequent charge-balance substitution of magnesium for titanium in M1-site (Dolfi and Trigila, 1983; Mollo et al., 2020). Hourglass forms are also enriched in  ${}^T\text{Si}$  and  ${}^{M1}\text{Mg}$ , whereas prism forms are preferentially enriched in  ${}^T\text{Al}$  and  ${}^{M1}\text{Ti}$ , in accord with

previous natural (Di Stefano et al., 2020; Downes, 1974; Duncan and Preston, 1980; Petrone et al., 2022; Ubide et al., 2019) and experimental (MacDonald et al., 2022; Masotta et al., 2020; Moschini et al., 2021) observations on augitic clinopyroxene crystals growing from undercooled alkaline melts, typical of open-conduit volcanoes in Italy. In terms of clinopyroxene components, the sum of diopside and hedenbergite (DiHd) decreases with increasing  $\Delta T_{anh/hyd}$  (Fig. 3). An opposite trend is also found for the sum of Ca-Tschermak and CaTi-Tschermak (Ts) components. As expected, the solubility of Ts increases in crystals formed under hydrous crystallization conditions. No clear variations are observed for jadeite (Jd) and sum of enstatite and ferrosilite (EnFs) (Fig. 3).

Anorthite in plagioclase increases from 0.59 to 0.73 mol% with decreasing  $\Delta T_{anh}$ , and from 0.69 to 0.74 mol% with decreasing  $\Delta T_{hyd}$  (Table S3 in the Supplementary Material 2). The effect of dissolved H<sub>2</sub>O enlarges the stability of anorthite component in the lattice site of plagioclase.

According to the TAS (total alkali vs. silica; Bas et al., 1986) classification diagram (Fig. 4a), the starting melt composition evolves from basalt ( $\Delta T_{hyd} \leq 25$  °C) to basaltic trachy-andesite ( $\Delta T_{hyd} = 50$ –125 °C and  $\Delta T_{anh} = 25$ –100 °C) to trachyandesite ( $\Delta T_{anh} = 150$  °C). Notably, for a fixed degree of undercooling, experimental glasses obtained at  $\Delta T_{hyd}$  are more enriched in CaO and depleted in MgO than those obtained at  $\Delta T_{anh}$  (Fig. 4b, c; Table S1 in the Supplementary Material 2) mainly reflecting the dominant proportion of clinopyroxene over plagioclase under hydrous crystallization conditions (Table 1).

## 4. Discussion

### 4.1. Control of undercooling on clinopyroxene morphological evolution

BSE (Fig. 1) and SR- $\mu$ CT (Fig. 2) images from this work document that the texture of clinopyroxene remarkably changes upon the effect of  $\Delta T_{anh/hyd}$ . Sector-zoned clinopyroxene crystals with flat faces and polyhedral morphologies develop at  $\Delta T_{anh/hyd} \leq 50$  °C (Fig. 1a,b,d,e), as the result of a layer-by-layer growth mechanism governed by an interface-controlled crystallization regime (Masotta et al., 2020; Ubide et al., 2019). Therefore, the growth rate of sector-zoned crystals must be slow to attain time-equivalent planar surfaces that form crystallographically nonequivalent faces. The three-dimensional geometry of polyhedral faces corresponds to the morphological model reported in Leung (1974) for a natural titanaugite from an alkaline olivine basalt. Prism sectors grow perpendicular to the *c*-axis and are preferentially enriched in <sup>T</sup>Al and <sup>M1</sup>Ti, whereas hourglass sectors grow along the *c*-axis and incorporate higher proportions of <sup>T</sup>Si and <sup>M1</sup>Mg. Sectoral partitioning depends on the two-dimensional atomic arrangements of the growing layers, whereas the overall three-dimensional nearest-neighbor coordination remains essentially unchanged (Dowty, 1976; Ferguson, 1973; Hollister and Gancarz, 1971; Leung, 1974; Nakamura, 1973; Shimizu, 1981). Because the activation energy for crystal growth in the system CaMgSi<sub>2</sub>O<sub>6</sub>-CaAl<sub>2</sub>SiO<sub>6</sub> increases with increasing the number of non-essential structural constituents in the adsorption layer (e.g., Al and Ti as impurity cations), this gives reason for the fast growth of Al-Ti-poor hourglass faces and the slow growth of Al-Ti-rich of prism faces (Kirkpatrick, 1975). Furthermore, to maintain the prismatic habit and morphological stability at  $\Delta T_{anh/hyd} \leq 50$  °C, the ratio between length (*L*) and width (*W*) of the sector-zoned crystal must be constant at all stages of growth, with hourglass forms being faster-growing than prism forms to increase the size of the prismatic habit along the *c*-axis direction (Ferguson, 1973; Hollister and Gancarz, 1971; Leung, 1974; Nakamura, 1973).

In contrast, the attainment of dendritic and skeletal morphologies at  $\Delta T_{anh/hyd} \geq 75$  °C (Fig. 1c,f) testifies to the establishment of diffusion-limited reactions at the crystal-melt interface and consequent morphological instability. Dendritic branches form at the early-stage of cooling due to high degree of disequilibrium caused by moderately to highly

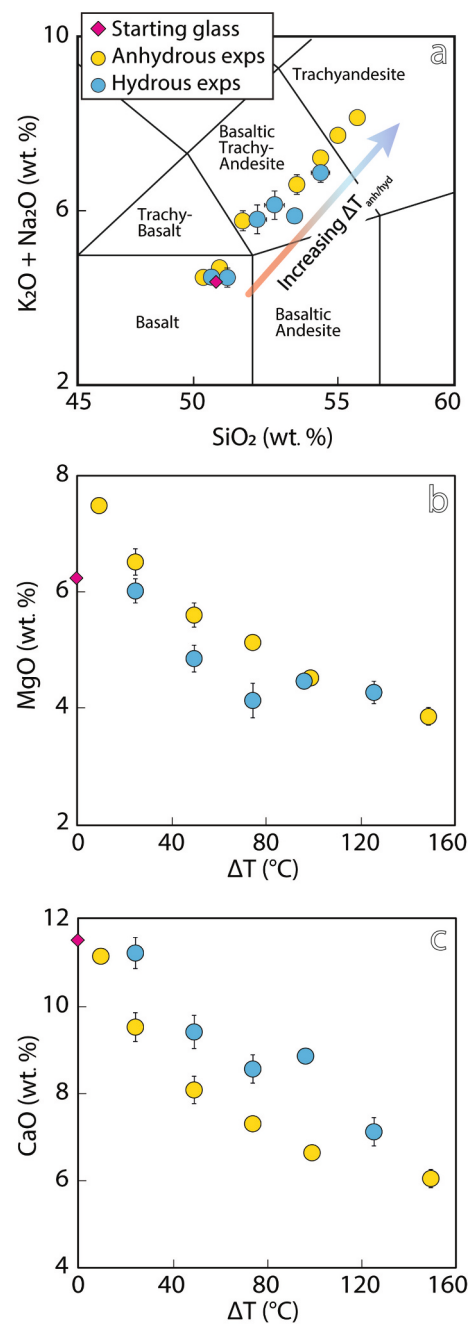


**Fig. 4.** Compositional changes of major elements in experimental glasses obtained at varying degrees of  $\Delta T_{anh}$  (yellow circles) and  $\Delta T_{hyd}$  (blue circles) plotted in the total alkali vs. silica diagram (a) (Bas et al., 1986); diagrams showing the variation of MgO and CaO (wt%) vs.  $\Delta T$  (b,c). The composition of the starting glass is also reported for comparison (red diamond). (For interpretation of the references to colour in this figure legend, the reader is referred to the web version of this article.)

supersaturated melts (Kirkpatrick, 1975). As the crystal growth rate and chemical gradients in the melt diminish with progressing annealing time (Masotta et al., 2020; Pontesilli et al., 2019), dendritic branches are infilled by more relaxed melts (Fig. 2a,b). In this late stage, the transition between diffusion-limited to interface-limited growth regime leads to the formation of skeletal overgrowths (Fig. 2a,b). Our interpretation is consistent with novel data for crystal growth kinetics obtained by Arzilli et al. (2022) using in situ 4D (three spatial dimensions plus time) X-ray  $\mu$ CT experiments. The authors illustrate that the formation of elongate crystal frameworks can be progressively infilled by further overgrowth

stages as the crystal growth rate decays with time. [Arzilli et al. \(2022\)](#) quantify that the growth rate profile of a single dendrite initially accelerates rapidly to a maximum of  $10^{-5}$  cm/s and then decelerates to  $10^{-7}$  cm/s as the crystal approaches its final equilibrium size. Crystallographic branching is the preferred growth mechanism that triggers rapid dendritic growth, with minor effects ascribed to non-crystallographic branching during diffusion-limited growth. A crystallographic-oriented growth can be explained by the fact that the thickness of the diffusion field in the melt is minimum at the crystal corners, so that the rapidly growing dendrites can penetrate the diffusion field enriched in non-essential structural constituents and thus sample fresh melt without the need for long-range diffusion ([Walker et al., 1976](#)).

An initial acceleration of crystal growth in our experiments is suggested by the formation of vesicles in close proximity to dendritic clinopyroxene branches developed at  $\Delta T_{hyd} \geq 75$  °C ([Figs. 1f and 2a,b](#)). Owing to the imbalance between crystal growth velocity and H<sub>2</sub>O diffusion in the melt, vesicle nucleation at the crystal-melt interface is expected to occur upon the establishment of a concentration gradient (i. e., H<sub>2</sub>O is highly incompatible in clinopyroxene lattice; [O'Leary et al., 2010](#)) and subsequent achievement of H<sub>2</sub>O supersaturation in the melt. Recent in situ experimental observations of vesicle nucleation in silicate melts at high temperature ([Masotta et al., 2014](#); [Pleše et al., 2018](#)) support the hypothesis that fast-growing dendrites provided the substrate for heterogeneous vesicle nucleation in the melt, energetically more favoured compared to homogeneous nucleation (otherwise not observed in the experiments).

At  $\Delta T_{anh/hyd} \geq 95$  °C, we also note that strong melt supersaturation produces rosette-like structures composed of dendritic branches radiating from a common spinel crystal acting as heterogeneous nucleation center ([Fig. 2c,d](#)). The nucleation process on a foreign substrate is facilitated by the lower work for critical cluster formation and the higher cation diffusivity in depolymerized melts ([Fokin et al., 2006](#)). The three-dimensional arrangement of clinopyroxene and spinel may result from surface energy minimization due to crystallographic alignment and epitaxy, as suggested by [Hammer et al. \(2010\)](#). Heterogeneous nucleation followed by epitaxial crystal growth leads to strong crystallographic preferred orientation of clinopyroxene and spinel, followed by differential rotation of clinopyroxene dendrites when compositional boundary layers from neighbouring branches impinge to one another ([Hammer et al., 2010](#)). A rosette-like structure develops when clinopyroxene branches inclined to the spinel surface at the center of the crystal framework will make contact with other clinopyroxene branches growing perpendicularly and stop their growth ([Sunagawa, 2005](#)). In this context, only the dendritic branches growing perpendicularly to the spinel surface will survive and continue to grow. Branching growth will be promoted further by strong melt supersaturation and will be accompanied by a decrease in the number of single individual crystals and appearance of connected dendrite arms aligned in a radial orientation ([Fig. 2c,d](#)).

Natural analogues of the dendritic structures produced experimentally can be observed in combustion metamorphic rocks ([Grapes, 2011](#)), komatiitic lavas ([Faure et al., 2006](#)) and basaltic fulgurites ([Griffiths et al., 2023](#)). In this latter example, EBSD data indicate higher dislocation densities in the crystal lattice of dendrites with higher bending angles, interpreted as due to high degrees of undercooling reached during the formation of these rocks. According to the same authors, the preservation of high dislocation densities and bended geometry can be attributed to a very fast quench (as typical of the fulgurite formation process), which explains the uncommon occurrence of similar structures in basaltic rocks.

#### 4.2. Clinopyroxene-based parametrization of the undercooling

The transition from an interface limited to a diffusion limited growth regime upon the effect of  $\Delta T_{anh/hyd}$  favours the incorporation of slow-

diffusing <sup>T</sup>Al and <sup>M1</sup>Ti cations in clinopyroxene lattice site ([Fig. 3](#)). In spite of this large chemical variability, crystals result in equilibrium with the co-existing silicate melt (Table S4 in the Supplementary Material 2), when tested with the model reappraised by [Mollo et al. \(2013\)](#) and based on the early formalism of [Putirka \(1999\)](#). This model is based on the difference between Di and Hd ( $\Delta DiHd$ ) components predicted for clinopyroxene via regression analysis of clinopyroxene-melt pairs in equilibrium conditions, and those measured in the analysed crystals. From a theoretical point of view, the equilibrium condition is achieved when the value of  $\Delta DiHd$  is within 0.10 ([Mollo and Masotta, 2014](#)). The only exception is represented by crystal-melt pairs from the experiment carried out at  $\Delta T_{anh} = 150$  °C (Table S4 in the Supplementary Material 2), due to the combined effects of a large degree of undercooling and slow cation mobility in the anhydrous melt. The condition of a local interface equilibrium (i.e., equilibrium of a reaction in a small volume) at the clinopyroxene-melt interface independently of melt supersaturation supports the achievement of a steady-state diffusive mass transport in high-temperature, low-viscosity basaltic melts ([Lang et al., 2021, 2022](#)).

According to [Fig. 3](#) we consider the following kinetically-controlled cation exchange reaction of clinopyroxene as a proxy for the estimate of  $\Delta T_{anh/hyd}$  under naturally solidification conditions:



On the basis of [Eq. \(1\)](#), a simple least squares regression model for the parameterization of  $\Delta T_{anh/hyd}$  as a function of clinopyroxene composition is derived:

$$\Delta T_{anh/hyd} (\text{°C}) = -12.3(\pm 17.3) + 684.6(\pm 137.9) \times \frac{{}^T\text{Al} + {}^{\text{M1}}\text{Ti}}{{}^T\text{Si} + {}^{\text{M1}}\text{Mg}} \quad (2)$$

where the <sup>M1</sup>Mg regression parameter represents the Mg cation fraction in the M1 site as described by [Wood and Blundy \(1997\)](#) for the thermodynamic treatment of the exchange reaction indicated by [Eq. \(1\)](#) (see Table S4 in the Supplementary Material 2). In spite of the large standard error (SE) on the regression parameters, which can result into a maximum variation of the  $\Delta T$  prediction of 26 °C, the [Eq. \(2\)](#) returns a reasonable standard error of estimate (SEE) of 15.2 °C and a coefficient of determination ( $R^2$ ) of 0.77 ([Fig. 5](#)). For the calibration of [Eq. \(2\)](#) we selected only the analyses of hourglass forms, as these compositions are an effective indicator of sluggish kinetic effects ([Masotta et al., 2020](#)). This choice allows to minimize the error of estimate of [Eq. \(2\)](#) associated with low degrees of undercooling recorded by clinopyroxene phenocrysts at pre-eruptive conditions, prior to the dynamic ascent of magma within the volcanic conduit and consequent fast microlite growth under large degrees of undercooling (i.e.,  $10^{-7}$ – $10^{-5}$  cm/s at  $\Delta T_{anh/hyd} > 30$  °C; [Arzilli et al., 2019, 2022](#); [Masotta et al., 2020](#); [Moschini et al., 2021](#)).

#### 4.3. Applications to magma dynamics at Stromboli volcano

In order to provide an application of [Eq. \(2\)](#) to eruptive products of normal and violent explosions at Stromboli, we compare the stoichiometry of augitic crystals from this study with that of diopsidic and augitic compositions of zoned phenocrysts erupted at Stromboli during the 2003–2019 activity (data from [Di Stefano et al., 2020](#) and [Petrone et al., 2022](#)). In [Fig. 6](#), the amount of <sup>T</sup>Si + <sup>M1</sup>Mg is plotted against <sup>T</sup>Al + <sup>M1</sup>Ti showing three different trends for experimental and natural crystals, together with results from linear regression analysis conducted on the different data sets. As expected, augitic experimental crystals do not capture in full the stoichiometric content of cations in diopsidic antecryst cores and recharge bands in natural phenocrysts ([Fig. 6](#)). This comparison indicates that [Eq. \(2\)](#) is not suitable to estimate the undercooling path of more primitive and hotter *Lp*-magmas injecting into the shallow *Hp*-reservoir at Stromboli, where diopsidic antecryst cores are remobilized and diopsidic recharge bands develop by *Lp*-*Hp* magma mixing ([Di Stefano et al., 2020](#); [Petrone et al., 2022](#)). Furthermore,

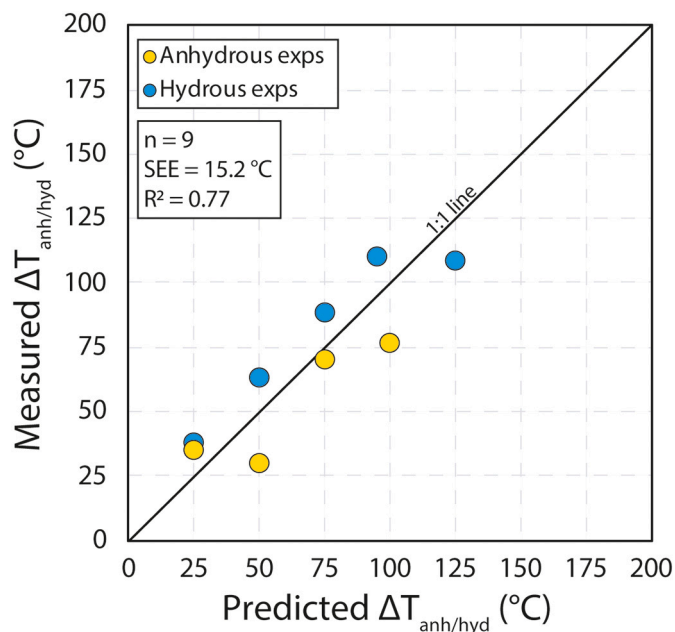


**Fig. 5.** Experimental calibration of the degree of undercooling ( $\Delta T_{anh/hyd}$ ) based on the  $[^T\text{Si} + ^{M1}\text{Mg}] \leftrightarrow [^T\text{Al} + ^{M1}\text{Ti}]$  exchange reaction, as determined from anhydrous (yellow circles) and hydrous (blue circles) experiments. The predicted  $\Delta T$  values (independent variable) are reported on the x-axis and the measured  $\Delta T$  values (dependent variable) on the y-axis (cfr. [Fabbriano and Spillar, 2020](#)). (For interpretation of the references to colour in this figure legend, the reader is referred to the web version of this article.)

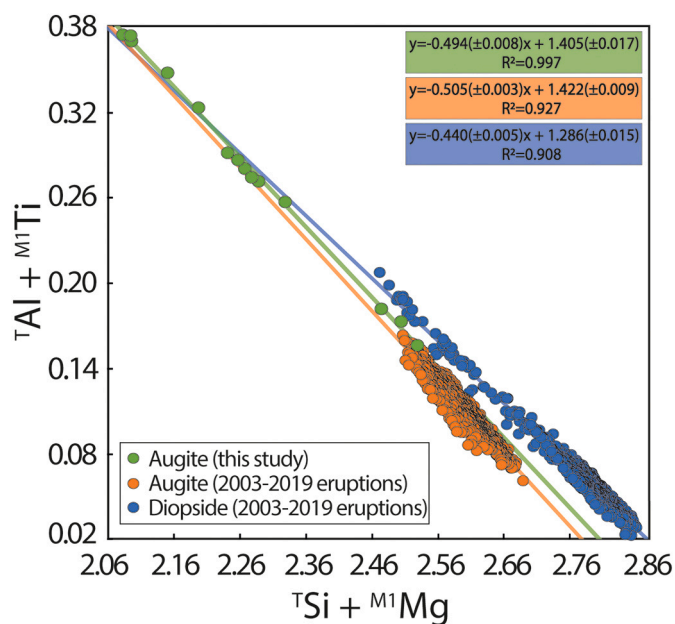


**Fig. 6.** Diagram showing the  $[^T\text{Si} + ^{M1}\text{Mg}]$  vs  $[^T\text{Al} + ^{M1}\text{Ti}]$  variation of experimental clinopyroxene crystals (augite, green circles) and natural zoned clinopyroxene crystals (augite, orange circles; diopside, blue circles) erupted at Stromboli volcano during the 2003–2019 eruptions (data from [Petroni et al., 2022](#) and [Di Stefano et al., 2020](#)). Linear regression analyses show three distinct trends for experimental and natural crystals. (For interpretation of the references to colour in this figure legend, the reader is referred to the web version of this article.)

augitic crystals from this study are generally more enriched in  $^T\text{Al} + ^{M1}\text{Ti}$  and depleted in  $^T\text{Si} + ^{M1}\text{Mg}$  than augitic overgrowths (mantles and rims) that crystallize into the shallow *Hp*-reservoir ([Fig. 6](#)). Our experimental crystals are compositionally more evolved than augitic overgrowths, even when the degree of crystallization is relatively low due to high thermal conditions (i.e., 16–24 vol% and 1150–1175 °C, respectively; [Table 1](#)). Therefore, we speculate that the composition of augitic overgrowths at Stromboli is strongly mediated by the periodic supply of fresh *Hp*-magma in the uppermost section of the plumbing system, in combination with efficient mixing phenomena that limit the geochemical evolution of clinopyroxene into the *Hp*-reservoir ([Di Stefano et al., 2020](#); [Petroni et al., 2022](#)). However, within the standard errors of regression coefficients, both slope ( $0.494 \pm 0.008$ ) and intercept ( $1.405 \pm 0.017$ ) of experimental trend match with those ( $0.505 \pm 0.003$  and  $1.422 \pm 0.009$ , respectively) obtained for the augitic overgrowths ([Fig. 6](#)), thereby suggesting that extrapolation of experimental data to natural compositions is possible with a good approximation for the augite counterpart.

According to the above considerations, we have selected the analyses of augitic mantles and rims from clinopyroxene crystals erupted during the normal (2017) and violent (2007) explosions at Stromboli as test data for Eq. (2) ([Table S5](#) in the Supplementary Material 2; data from [Di Stefano et al., 2020](#)). In [Fig. 7](#), values of  $\Delta T_{anh/hyd}$  predicted by our model are plotted against the temperatures estimated by the clinopyroxene-based thermometer by [Scarlato et al. \(2021\)](#) (specifically calibrated to Stromboli magmas and with an error of  $\pm 6$  °C), along with their Kernel density functions showing the distribution of both  $T$  and  $\Delta T_{anh/hyd}$  values. We found that augitic overgrowths align along two different  $T$ - $\Delta T_{anh/hyd}$  trends resulting from the fact that violent explosions are triggered by the supply of statistically hotter and more undercooled magmas than those feeding normal eruptions. This interpretation is supported by the number of clinopyroxene from normal eruptions yielding a maximum density of  $\Delta T_{anh/hyd}$  values at about 10 °C, interpretable as the result of crystallization upon nearly isothermal conditions and consequent sluggish growth kinetics that limit the incorporation  $^T\text{Al}$  and  $^{M1}\text{Ti}$

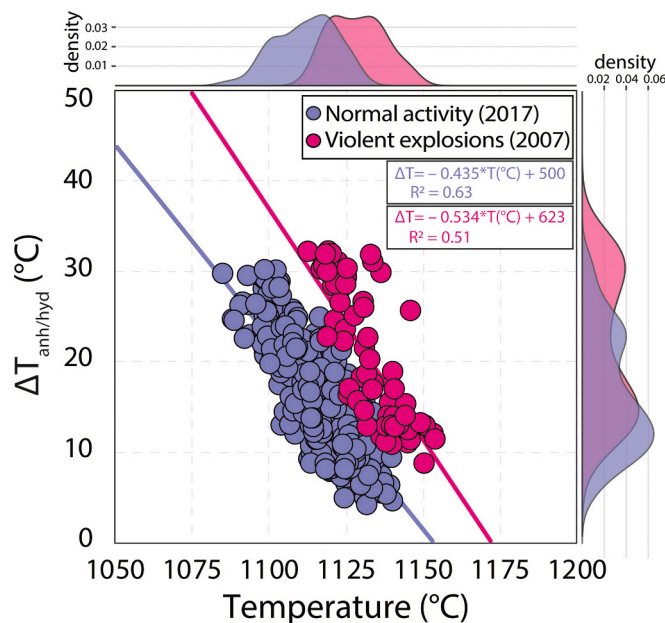


**Fig. 7.** Application of the  $\Delta T$  predictive model to the augitic mantles and rims from normal (2017) and violent (2007) explosions at Stromboli (data from [Di Stefano et al., 2020](#)). The calculated  $\Delta T$  values are compared to temperature estimates obtained using the predictive model of [Scarlato et al. \(2021\)](#), defining distinctive trends for the two types of eruptions. The Kernel density plots on the side of the diagram show the distribution of  $\Delta T$  and  $T$  values for the clinopyroxene population.

within the lattice site of clinopyroxene (cf. Mollo et al., 2015). Conversely, violent explosions at Stromboli are driven by sustained influxes of recharge magmas favoring strong acceleration, decompression, and H<sub>2</sub>O exsolution before magma discharge at the vent (Gauthier et al., 2000; La Spina et al., 2015, 2016; Landi et al., 2006, 2008; Métrich et al., 2001, 2010; Pichavant et al., 2022). Therefore, augitic overgrowths from violent explosions are heralds of a more rapid ascent path of magma through the conduit, where the crystallization process is more efficiently related to chemically- and thermally-induced growth kinetics caused by larger degrees of undercooling.

## 5. Conclusions

Undercooling crystallization experiments were performed to constrain the textural and compositional evolution of augitic clinopyroxene crystals growing from a high-K basalt erupted at Stromboli volcano on 5th April 2003. At high degrees of undercooling ( $\Delta T_{anh/hyd} \geq 95$  °C), anhedral crystals exhibit an inner domain characterized by dendritic branching growth and an outer domain characterized by skeletal morphologies resulting from melt relaxation effects proceeding over the annealing time. Rosette-like structures also develop in response to the heterogeneous nucleation of clinopyroxene on spinel, as the energetic barrier for the formation of a critical nucleus decreases due to the presence of a catalyst surface. In contrast, at low degrees of undercooling ( $\Delta T_{anh/hyd} = 25\text{--}50$  °C), euhedral sector-zoned clinopyroxene crystals show a characteristic enrichment of <sup>T</sup>Si + <sup>M1</sup>Mg and depletion of <sup>T</sup>Al + <sup>M1</sup>Ti in hourglass forms relative to prism forms. The compositional evolution of clinopyroxene is strongly controlled by the effect of growth kinetics, so that the degree of undercooling can be parameterized according to the exchange reaction  $[^T\text{Si} + ^{M1}\text{Mg}]_{\text{slow } \Delta T_{anh/hyd}} \leftrightarrow [^T\text{Al} + ^{M1}\text{Ti}]_{\text{fast } \Delta T_{anh/hyd}}$ . Application of this model to augitic clinopyroxene crystal populations erupted at Stromboli during normal activity and violent explosions allows to estimate the undercooling path of magmas during their dynamic ascent within the volcanic conduit.

## Declaration of Competing Interest

The authors declare that they have no known competing financial interests or personal relationships that could have appeared to influence the work reported in this paper.

## Acknowledgement

The authors are grateful to Greg Shellnutt, Editor-in-Chief of Lithos and to the two anonymous reviewers for their valuable comments. We acknowledge Elettra Sincrotrone Trieste for providing access to its synchrotron radiation facilities. This work was supported by the MIUR project “Time scales of solidification in magmas: Applications to Volcanic Eruptions, Silicate Melts, Glasses, Glass-Ceramics” (PRIN 2017J277S9) to MM, AP and SM.

## Appendix A. Supplementary data

Supplementary data to this article can be found online at <https://doi.org/10.1016/j.lithos.2023.107327>.

## References

- Armentieri, P., Perinelli, C., Putirka, D.K., 2013. A new model to estimate deep-level magma ascent rates, with applications to Mt. Etna (Sicily, Italy). *J. Petrol.* 54 (4), 781–795.
- Arzilli, F., Agostini, C., Landi, P., Fortunati, A., Mancini, L., Carroll, M.R., 2015. Plagioclase nucleation and growth kinetics in a hydrous basaltic melt by decompression experiments. *Contrib. Mineral. Petrol.* 170, 55.
- Arzilli, F., La Spina, G., Burton, M.R., Polacci, M., Le Gall, N., Hartley, M.E., Di Genova, D., Cai, B., Vo, N.T., Bamber, E.C., Nonni, S., Atwood, R., Llewellyn, E.W., Brooker, R.A., Mader, H.M., Lee, P.D., 2019. Magma fragmentation in highly explosive basaltic eruptions induced by rapid crystallization. *Nat. Geosci.* 12, 1023–1028.
- Arzilli, F., Polacci, M., La Spina, G., Le Gall, N., Llewellyn, E.W., Brooker, R.A., Torres-Orozco, R., Di Genova, D., Neave, D.A., Hartley, M.E., Mader, H.M., Giordano, D., Atwood, R., Lee, P.D., Heidelbach, F., Burton, M.R., 2022. Dendritic crystallization in hydrous basaltic magmas controls magma mobility within the Earth’s crust. *Nat. Commun.* 13, 1–14.
- Bas, M.L., Maitre, R.L., Streckeisen, A., Zanettin, B., IUGS Subcommittee on the Systematics of Igneous Rocks, 1986. A chemical classification of volcanic rocks based on the total alkali-silica diagram. *J. Petrol.* 27 (3), 745–750.
- Bertagnini, A., Métrich, N., Landi, P., Rosi, M., 2003. Stromboli volcano (Aeolian Archipelago, Italy): an open window on the deep-feeding system of a steady state basaltic volcano. *J. Geophys. Res. Solid Earth* 108 (B7).
- Bertagnini, A., Métrich, N., Francalanci, L., Landi, P., Tommasini, S., Conticelli, S., 2008. Volcanology and magma geochemistry of the present-day activity: constraints on the feeding system. In: *The Stromboli Volcano: an Integrated Study of the 2002–2003 Eruption*, 182, pp. 19–37.
- Brun, F., Pacilé, S., Kourousias, G., Dreossi, D., Mancini, L., Tromba, G., Pugliese, R., 2015. Enhanced and flexible software tools for X-ray tomography experiments at the Italian synchrotron radiation facility Elettra. *Fundam. Inform.* 141, 233–243.
- Coish, R.A., Taylor, L.A., 1979. The effects of cooling rate on texture and pyroxene chemistry in DSDP Leg 34 basalt: a microprobe study. *Earth Planet. Sci. Lett.* 42 (3), 389–398.
- Costa, S., Caricchi, L., Pistolesi, M., Gioncada, A., Masotta, M., Bonadonna, C., Rosi, M., 2023. A data driven approach to mineral chemistry unveils magmatic processes associated with long-lasting, low-intensity volcanic activity. *Sci. Rep.* 13 (1), 1314.
- Di Fiore, F., Vona, A., Costa, A., Mollo, S., Romano, C., 2022. Quantifying the influence of cooling and shear rate on the disequilibrium rheology of a trachybasaltic melt from Mt. Etna. *Earth Planet. Sci. Lett.* 594, 117725.
- Di Stefano, F., Mollo, S., Ubide, T., Petrone, C.M., Caulfield, J., Scarlato, P., Nazzari, M., Andronico, D., Del Bello, E., 2020. Mush cannibalism and disruption recorded by clinopyroxene phenocrysts at Stromboli volcano: new insights from recent 2003–2017 activity. *Lithos* 360–361.
- Dolfi, D., Trigila, R., 1983. Clinopyroxene solid solutions and water in magmas: results in the system phonolitic tephrite-H<sub>2</sub>O. *Mineral. Mag.* 47 (344), 347–351.
- Downes, M.J., 1974. Sector and oscillatory zoning in calcic augites from M. Etna, Sicily. *Contrib. Mineral. Petrol.* 47 (3), 187–196.
- Dowty, E., 1976. Crystal structure and crystal growth; II, sector zoning in minerals. *Am. Mineral.* 61 (5–6), 460–469.
- Duncan, A.M., Preston, R.M.F., 1980. Chemical variation of clinopyroxene phenocrysts from the trachybasaltic lavas of Mount Etna, Sicily. *Mineral. Mag.* 43 (330), 765–770.
- Fabbrizio, A., Špillar, V., 2020. Methodology to derive well-calibrated thermometers; a new glass-composition geothermometer for olivine-bearing glassy samples at one atmosphere. *Ann. Geophys.* 63 (4).
- Faure, F., Arndt, N., Libourel, G., 2006. Formation of spinifex texture in komatiites: an experimental study. *J. Petrol.* 47 (8), 1591–1610.
- Ferguson, A.K., 1973. On hour-glass sector zoning in clinopyroxene. *Mineral. Mag.* 39 (303), 321–325.
- Fokin, V.M., Zannotto, E.D., Yuritsyn, N.S., Schmelzer, J.W., 2006. Homogeneous crystal nucleation in silicate glasses: a 40 years perspective. *J. Non-Cryst. Solids* 352 (26–27), 2681–2714.
- Francalanci, L., Tommasini, S., Conticelli, S., 2004. The volcanic activity of Stromboli in the 1906–1998 AD period: mineralogical, geochemical and isotope data relevant to the understanding of the plumbing system. *J. Volcanol. Geotherm. Res.* 131, 179–211.
- Francalanci, L., Avanzinelli, R., Nardini, I., Tiepolo, M., Davidson, J.P., Vannucci, R., 2012. Crystal recycling in the steady-state system of the active Stromboli volcano: a 2.5-ka story inferred from in situ Sr-isotope and trace element data. *Contrib. Mineral. Petrol.* 163, 109–131.
- Gamble, R.P., Taylor, L.A., 1980. Crystal/liquid partitioning in augite: effects of cooling rate. *Earth Planet. Sci. Lett.* 47 (1), 21–33.
- Gauthier, P.J., Le Cloarec, M.F., Condomines, M., 2000. Degassing processes at Stromboli volcano inferred from short-lived disequilibria (210Pb–210Bi–210Po) in volcanic gases. *J. Volcanol. Geotherm. Res.* 102, 1–19.
- Ghiorso, M.S., Sack, R.O., 1995. Chemical mass transfer in magmatic processes IV. A revised and internally consistent thermodynamic model for the interpolation and extrapolation of liquid-solid equilibria in magmatic systems at elevated temperatures and pressures. *Contrib. Mineral. Petrol.* 119, 197–212.
- Grapes, R., 2011. *Pyrometamorphism*. Springer, Germany, p. 377.
- Griffiths, T.A., Habler, G., Ageeva, O., Sutter, C., Ferrière, L., Abart, R., 2023. The origin of lattice rotation during dendritic crystallization of clinopyroxene. *J. Petrol.* 64 (1), egac125.
- Gualda, G.A., Ghiorso, M.S., Lemons, R.V., Carley, T.L., 2012. Rhyolite-MELTS: a modified calibration of MELTS optimized for silica-rich, fluid-bearing magmatic systems. *J. Petrol.* 53, 875–890.
- Hammer, J.E., 2006. Influence of *f*O<sub>2</sub> and cooling rate on the kinetics and energetics of Fe-rich basalt crystallization. *Earth Planet. Sci. Lett.* 248, 618–637.
- Hammer, J.E., 2008. Experimental studies of the kinetics and energetics of magma crystallization. In: Putirka, K.D., Tepley, F.J. (Eds.), *Minerals, Inclusions and Volcanic Processes. Reviews in Mineralogy and Geochemistry*, 69, pp. 9–59.
- Hammer, J.E., Sharp, T.G., Wessel, P., 2010. Heterogeneous nucleation and epitaxial crystal growth of magmatic minerals. *Geology* 38 (4), 367–370.
- Hollister, L.S., Gancarz, A.J., 1971. Compositional sector-zoning in clinopyroxene from the narce area, Italy. *Am. Mineral.: J. Earth Planet. Mater.* 56 (5–6), 959–979.

- Jarosewich, E., Nelen, J.A., Norberg, J.A., 1980. Reference samples for electron microprobe analysis. *Geostand. Newslett.* 4 (1), 43–47.
- Kirkpatrick, R.J., 1975. Crystal growth from the melt: a review. *Am. Mineral.* 60, 798–814.
- Kirkpatrick, R.J., 1981. Kinetics of crystallization of igneous rocks. In: *Kinetics of Geochemical Processes*. De Gruyter, pp. 321–398.
- Kouchi, A., Sugawara, Y., Kashima, K., Sunagawa, I., 1983. Laboratory growth of sector zoned clinopyroxenes in the system  $\text{CaMgSi}_2\text{O}_6\text{-CaTiAl}_2\text{O}_6$ . *Contrib. Mineral. Petrol.* 83, 177–184.
- Kurokawa, A.K., Takahiro, M., Hidemi, I., 2022. Aging in magma rheology. *Sci. Rep.* 12, 10015.
- La Spina, G., Burton, M., Vitturi, M.D.M., 2015. Temperature evolution during magma ascent in basaltic effusive eruptions: a numerical application to Stromboli volcano. *Earth Planet. Sci. Lett.* 426, 89–100.
- La Spina, G., Burton, M., Vitturi, M.D.M., Arzilli, F., 2016. Role of syn-eruptive plagioclase disequilibrium crystallization in basaltic magma ascent dynamics. *Nat. Commun.* 7, 1–10.
- Landi, P., Francalanci, L., Pompilio, M., Rosi, M., Corsaro, A., Petrone, C.M., Nardini, I., Miraglia, L., 2006. The December 2002–July 2003 effusive event at Stromboli volcano, Italy: insights into the shallow plumbing system by petrochemical studies. *J. Volcanol. Geotherm. Res.* 155, 263–284.
- Landi, P., Métrich, N., Bertagnini, A., Rosi, M., 2008. Recycling and “re-hydration” of degassed magma inducing transient dissolution/crystallization events at Stromboli (Italy). *J. Volcanol. Geotherm. Res.* 174, 325–336.
- Landi, P., Corsaro, R.A., Francalanci, L., Civetta, L., Miraglia, L., Pompilio, M., Tesoro, R., 2009. Magma dynamics during the 2007 Stromboli eruption (Aeolian Islands, Italy): mineralogical, geochemical and isotopic data. *J. Volcanol. Geotherm. Res.* 182 (3–4), 255–268.
- Lang, S., Mollo, S., Lyderic, F., Misiti, V., Nazzari, M., 2021. Kinetic partitioning of major–minor cations between olivine and Hawaiian tholeiitic basalt under variable undercooling and cooling rate conditions. *Chem. Geol.* 584, 120485.
- Lang, S., Mollo, S., Lyderic, F., Misiti, V., Nazzari, M., 2022. Partitioning of Ti, Al, P, and Cr between olivine and a tholeiitic basaltic melt: insights on olivine zoning patterns and cation substitution reactions under variable cooling rate conditions. *Chem. Geol.* 601, 120870.
- Lasaga, A.C., 1998. Theory of crystal growth and dissolution. In: *Kinetic Theory in the Earth Sciences*, pp. 581–712.
- Leung, I.S., 1974. Sector-zoned titanaugetes: morphology, crystal chemistry, and growth. *Am. Mineral.: J. Earth Planet. Mater.* 59 (1–2), 127–138.
- Lofgren, G.E., Huss, G.R., Wasserburg, G.J., 2006. An experimental study of trace-element partitioning between Ti–Al–clinopyroxene and melt: Equilibrium and kinetic effects including sector zoning. *Am. Mineral.* 91 (10), 1596–1606.
- MacDonald, A., Ubide, T., Mollo, S., Masotta, M., Pontesilli, A., 2022. Trace element partitioning in zoned clinopyroxene as a proxy for undercooling: experimental constraints from trachybasaltic magmas. *Geochim. Cosmochim. Acta* 336, 249–268.
- Masotta, M., Freda, C., Paul, T.A., Moore, G.M., Gaeta, M., Scarlato, P., Troll, V.R., 2012. Low pressure experiments in piston cylinder apparatus: calibration of newly designed 25 mm furnace assemblies to  $P=150$  MPa. *Chem. Geol.* 312, 74–79.
- Masotta, M., Ni, H., Keppler, H., 2014. In situ observations of bubble growth in basaltic, andesitic and rhyodacitic melts. *Contrib. Mineral. Petrol.* 167, 967.
- Masotta, M., Pontesilli, A., Mollo, S., Armienti, P., Ubide, T., Nazzari, M., Scarlato, P., 2020. The role of undercooling during clinopyroxene growth in trachybasaltic magmas: insights on magma decompression and cooling at Mt. Etna volcano. *Geochim. Cosmochim. Acta* 268, 258–276.
- McKay, G., Le, L., Wagstaff, J., Crozaz, G., 1994. Experimental partitioning of rare earth elements and strontium: constraints on petrogenesis and redox conditions during crystallization of Antarctic angrite Lewis Cliff 86010. *Geochim. Cosmochim. Acta* 58 (13), 2911–2919.
- Métrich, H.N., Bertagnini, A., Landi, P., Rosi, M., Belhadji, O., 2005. Triggering mechanism at the origin of paroxysms at Stromboli (Aeolian Archipelago, Italy): the 5 April 2003 eruption. *Geophys. Res. Lett.* 32, L10305.
- Métrich, N., Bertagnini, A., Landi, P., Rosi, M., 2001. Crystallization driven by decompression and water loss at Stromboli volcano (Aeolian Islands, Italy). *J. Petrol.* 42, 1471–1490.
- Métrich, N., Bertagnini, A., Di Muro, A., 2010. Conditions of magma storage, degassing and ascent at Stromboli: new insights into the volcano plumbing system with inferences on the eruptive dynamics. *J. Petrol.* 51, 603–626.
- Mollo, S., Hammer, J., 2017. Dynamic crystallization in magmas. *E. M. U. Notes Mineral.* 16, 373–418.
- Mollo, S., Masotta, M., 2014. Optimizing pre-eruptive temperature estimates in thermally and chemically zoned magma chambers. *Chem. Geol.* 368, 97–103.
- Mollo, S., Del Gaudio, P., Ventura, G., Iezzi, G., Scarlato, P., 2010. Dependence of clinopyroxene composition on cooling rate in basaltic magmas: implications for thermobarometry. *Lithos* 118 (3–4), 302–312.
- Mollo, S., Putirka, K., Misiti, V., Soligo, M., Scarlato, P., 2013. A new test for equilibrium based on clinopyroxene–melt pairs: clues on the solidification temperatures of Etnean alkaline melts at post-eruptive conditions. *Chem. Geol.* 352, 92–100.
- Mollo, S., Blundy, J.D., Iezzi, G., Scarlato, P., Langone, A., 2013a. The partitioning of trace elements between clinopyroxene and trachybasaltic melt during rapid cooling and crystal growth. *Contrib. Mineral. Petrol.* 166, 1633–1654.
- Mollo, S., Putirka, K., Misiti, V., Soligo, M., Scarlato, P., 2013b. A new test for equilibrium based on clinopyroxene–melt pairs: clues on the solidification temperatures of Etnean alkaline melts at post-eruptive conditions. *Chem. Geol.* 352, 92–100.
- Mollo, S., Giacomoni, P.P., Andronico, D., Scarlato, P., 2015. Clinopyroxene and titanomagnetite cation redistributions at Mt. Etna volcano (Sicily, Italy): footprints of the final solidification history of lava fountains and lava flows. *Chem. Geol.* 406, 45–54.
- Mollo, S., Blundy, J., Scarlato, P., De Cristofaro, S.P., Tecchiato, V., Di Stefano, F., Vetere, F., Holtz, F., Bachmann, O., 2018. An integrated PT–H<sub>2</sub>O–lattice strain model to quantify the role of clinopyroxene fractionation on REE+Y and HFSE patterns of mafic alkaline magmas: application to eruptions at Mt. Etna. *Earth Sci. Rev.* 185, 32–56.
- Mollo, S., Blundy, J., Scarlato, P., Vetere, F., Holtz, F., Bachmann, O., Gaeta, M., 2020. A review of the lattice strain and electrostatic effects on trace element partitioning between clinopyroxene and melt: applications to magmatic systems saturated with Tschermak-rich clinopyroxenes. *Earth Sci. Rev.* 210, 103351.
- Mollo, S., Pontesilli, A., Moschini, P., Palummo, F., Taddeucci, J., Andronico, D., Del Bello, E., Scarlato, P., 2022. Modeling the crystallization conditions of clinopyroxene crystals erupted during February–April 2021 lava fountains at Mt. Etna: implications for the dynamic transfer of magmas. *Lithos* 420, 106710.
- Moschini, P., Mollo, S., Gaeta, M., Fanara, S., Nazzari, M., Petrone, C.M., Scarlato, P., 2021. Parameterization of clinopyroxene growth kinetics via crystal size distribution (CSD) analysis: insights into the temporal scales of magma dynamics at Mt. Etna volcano. *Lithos* 396, 106225.
- Nakamura, Y., 1973. Origin of sector-zoning of igneous clinopyroxenes. *Am. Mineral.: J. Earth Planet. Mater.* 58 (11–12), 986–990.
- O’Leary, J.A., Gaetani, G.A., Hauri, E.H., 2010. The effect of tetrahedral Al<sup>3+</sup> on the partitioning of water between clinopyroxene and silicate melt. *Earth Planet. Sci. Lett.* 297 (1–2), 111–120.
- Palummo, F., Mollo, S., Petrone, C.M., Ellis, B.S., De Astis, G., Nazzari, M., Scarlato, P., Bachmann, O., 2021. Decoding multiple zoning patterns in clinopyroxene phenocrysts at Vulcano Island: a record of dynamic crystallization through interconnected reservoirs. *Lithos* 406, 106517.
- Petrone, C.M., Braschi, E., Francalanci, L., Casalini, M., Tommasini, S., 2018. Rapid mixing and short storage timescale in the magma dynamics of a steady-state volcano. *Earth Planet. Sci. Lett.* 492, 206–221.
- Petrone, C.M., Mollo, S., Gertisser, R., Buret, Y., Scarlato, P., Del Bello, E., Andronico, D., Ellis, B., Pontesilli, A., De Astis, G., Giacomoni, P.P., Coltorti, M., Reagan, M., 2022. Magma recharge and mush rejuvenation drive paroxysmal activity at Stromboli volcano. *Nat. Commun.* 13 (1), 7717.
- Pichavant, M., Di Carlo, I., Pompilio, M., Le Gall, N., 2022. Timescales and mechanisms of paroxysm initiation at Stromboli volcano, Aeolian Islands, Italy. *Bull. Volcanol.* 84 (4), 36.
- Pleše, P., Higgins, M.D., Mancini, L., Lanzafame, G., Brun, F., Fife, J.L., Casselman, J., Baker, D.R., 2018. Dynamic observations of vesiculation reveal the role of silicate crystals in bubble nucleation and growth in andesitic magmas. *Lithos* 296–299, 532–546.
- Pontesilli, A., Masotta, M., Nazzari, M., Mollo, S., Armienti, P., Scarlato, P., Brenna, M., 2019. Crystallization kinetics of clinopyroxene and titanomagnetite growing from a trachybasaltic melt: new insights from isothermal time-series experiments. *Chem. Geol.* 510, 113–129.
- Putirka, K., 1999. Clinopyroxene+ liquid equilibria to 100 kbar and 2450 K. *Contrib. Mineral. Petrol.* 135, 151–163.
- Scarlato, P., Mollo, S., Petrone, C.M., Ubide, T., Di Stefano, F., 2021. Interpreting magma dynamics through a statistically refined thermometer: implications for clinopyroxene Fe–Mg diffusion modeling and sector zoning at Stromboli. In: *Crustal Magmatic System Evolution: Anatomy, Architecture, and Physico-Chemical Processes*, pp. 195–212.
- Shimizu, N., 1981. Trace element incorporation into growing augite phenocryst. *Nature* 289 (5798), 575–577.
- Sunagawa, I., 2005. Crystals. *Crystals* 308.
- Tsuchiyama, A., 1985. Crystallization kinetics in the system  $\text{CaMgSi}_2\text{O}_6\text{-CaAl}_2\text{Si}_2\text{O}_8$ : development of zoning and kinetics effects on element partitioning. *Am. Mineral.* 70 (5–6), 474–486.
- Ubide, T., Kamber, B., 2018. Volcanic crystals as time capsules of eruption history. *Nat. Commun.* 9, 326.
- Ubide, T., Mollo, S., Zhao, J., Nazzari, M., Scarlato, P., 2019. Sector-zoned clinopyroxene as a recorder of magma history, eruption triggers, and ascent rates. *Geochim. Cosmochim. Acta* 251, 265–283.
- Walker, D., Kirkpatrick, R.J., Longhi, J., Hays, J.F., 1976. Crystallization history of lunar picritic basalt samples 12002: phase equilibria and cooling rate studies. *Geol. Soc. Am. Bull.* 87, 646–656.
- Wood, B.J., Blundy, J.D., 1997. A predictive model for rare earth element partitioning between clinopyroxene and anhydrous silicate melt. *Contrib. Mineral. Petrol.* 129, 166–181.